



Cite this: *Phys. Chem. Chem. Phys.*,
2018, 20, 27510

Reactions of water with radical cations of guanine, 9-methylguanine, 2'-deoxyguanosine and guanosine: keto–enol isomerization, C8-hydroxylation, and effects of N9-substitution†

Yan Sun,^{ab} Wenjing Zhou,^a May Myat Moe^a and Jianbo Liu ^{*ab}

The reactions of D₂O with radical cations of guanine (9HG^{•+}), 9-methylguanine (9MG^{•+}), 2'-deoxyguanosine (dGuo^{•+}) and guanosine (Guo^{•+}) were studied in the gas phase, including measurements of reaction cross sections over a center-of-mass collision energy (E_{col}) range from 0.1 to 2.0 eV and computation of reaction pathways at DLPNO-CCSD(T)/aug-cc-pVTZ// ω B97XD/6-31+G(d,p). Reaction efficiencies of all radical cations are well below unity (~2% of collision rate), despite there being exoergic pathways. For each reactant ion, the energetically most favorable product channel corresponds to the formation of water complexes; however, this channel accounts for only 5% of the total cross section at the lowest E_{col} and becomes negligible at high E_{col} due to short complex lifetimes. The dominant product channel is H/D exchange that appears to be complex-mediated at low E_{col} , but switches to a direct mechanism and accompanies keto–enol isomerization of the guanine moiety when E_{col} increases. C8-hydroxylation, a minor yet the most biologically important channel, was observed for 9HG^{•+}; and its mechanism was elucidated in the presence of single and double water molecules, of which the second water eliminates the barrier for C8-addition *via* a proton shuttle mechanism. All reactions show strong dependence on radical structures, with overall reactivity being 9HG^{•+} \gg 9MG^{•+} > dGuo^{•+} \approx Guo^{•+}. The reaction dynamics of 9HG^{•+} and 9MG^{•+} with water were simulated at $E_{\text{col}} = 0.1$ eV using ω B97XD/6-31+G(d), to reveal complex formation at the early stage of the reaction and the effects of N9-substitution. Trajectory results suggest that the lack of a W9 complex (water bonded to N9–H) is responsible for the reduced reactivity of N9-substituted radical cations; but the relatively long-lived W16 complexes (water bonded to N1–H and C6–O) of dGuo^{•+} and Guo^{•+} may enhance keto–enol isomerization.

Received 27th August 2018,
Accepted 16th October 2018

DOI: 10.1039/c8cp05453c

rsc.li/pccp

1. Introduction

Among all DNA nucleobases, guanine (G) has the lowest oxidation potential (E° vs. NHE = 1.29 V for guanosine, 1.10–1.24 V for the guanine moiety of DNA, 1.42 V for adenosine, 1.6 V for deoxycytidine, and 1.7 V for thymidine)^{1,2} and in parallel the lowest adiabatic ionization energy (AIE = 7.75 eV for G, 8.27 eV for adenine, 8.66 eV for cytosine, and 8.82 eV for thymine)^{3,4} and thus represents a preferential target for oxidation and ionization over adenine and pyrimidine bases. This leads to

the formation of a guanine radical cation G^{•+} in DNA upon radiolysis,^{5,6} mono-⁷ and bi-photonic⁸ UV laser photolysis, chemical oxidation,⁹ electron transfer between metal complexes bound to DNA,¹⁰ electrocatalytic oxidation,^{11,12} and type I photooxidation.^{13,14} Pairing guanine with cytosine in double-stranded (ds) DNA further decreases its oxidation potential,^{15,16} forcing radical cations (holes) initially formed on other nucleobases to migrate through the duplex and eventually leading to the more stable G^{•+}.^{6,17}

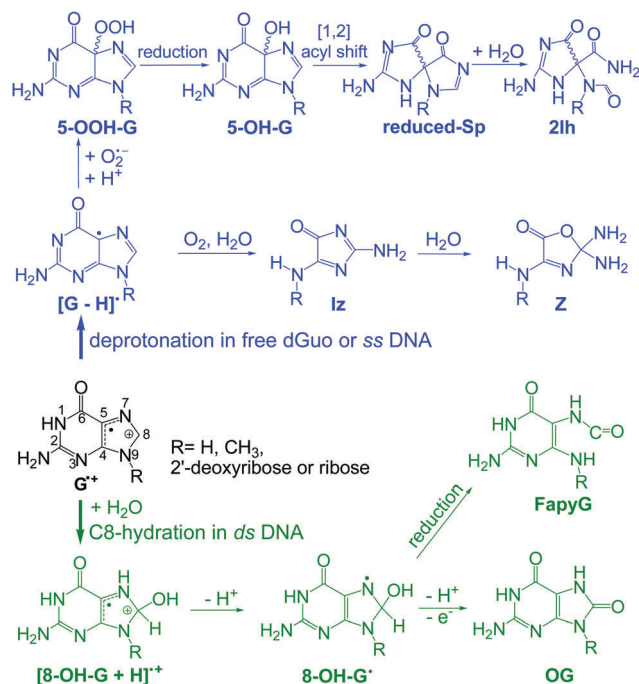
Scheme 1 outlines the intermediacy of G^{•+} in DNA post-ionization conversion.^{18–23} A unique feature of G^{•+} is that it becomes more acidic: *i.e.*, pK_a = 9.4 for guanosine and 3.9 for its radical cation.⁵ As a consequence, G^{•+} loses its N1-proton²⁴ to water at neutral pH within 56 ns (rate constant $k = 1.8 \times 10^7 \text{ s}^{-1}$).^{25,26} The resulting [G – H][•] does not directly react with water²⁷ and lives for 0.07–0.28 s in single-stranded (ss) DNA/oligonucleotide^{28,29} and for 0.18–5 s in ds DNA/oligonucleotides,^{29,30} before its conversion to 2Ih,²² Iz and Z,¹⁸ as depicted in Scheme 1. At low pH, the lifetime of G^{•+} is, in contrast,

^a Department of Chemistry and Biochemistry, Queens College of the City University of New York, 65-30 Kissena Blvd., Queens, NY 11367, USA.

E-mail: jianbo.liu@qc.cuny.edu; Tel: 1-718-997-3271

^b PhD Program in Chemistry, The Graduate Center of the City University of New York, 365 5th Ave., New York, NY 10016, USA

† Electronic supplementary information (ESI) available: Structures and Cartesian coordinates for 9HG^{•+}·(H₂O)_{0–1}, 9MG^{•+}·(H₂O)_{0–1}, dGuo^{•+}·(H₂O)_{0–1} and Guo^{•+}·(H₂O)_{0–1}, and for the reaction species in Fig. 2, 5 and 6. IRC trajectory videos for TS1-W and TS1-2W. See DOI: 10.1039/c8cp05453c



Scheme 1 Chemical transformations of guanine radical cation. Abbreviations: FapyG, 2,6-diamino-4-hydroxy-5-formamidopyrimidine; 2lh, 5-carboxamido-5-formamido-2-iminohydantoin; Iz, 2,5-diaminoimidazolone; OG, 8-oxo-7,8-dihydroguanine; 8-OH-G•, 8-hydroxylated guanine radical; Sp, spiroiminodihydantoin; Z, 2,2,4-triamino-2H-oxazol-5-one.

governed by C8–water addition, leading to the formation of a C8-hydroxylated guanine radical $[8\text{-OH-G} + \text{H}]^{\bullet+}$ —an intermediate that was proposed on the basis of the EPR/electron nuclear double resonance (ENDOR) measurement upon OH^\bullet addition to a single crystal of N7-protonated guanine.³¹ C8-hydroxylation is completed within 3 ms ($k = 3.3 \times 10^2 \text{ s}^{-1}$ at pH 2.5),²⁸ followed by secondary oxidation to 8-oxo-7,8-dihydroguanine (OG, $k = 4 \times 10^9 \text{ s}^{-1}$).^{19,20} OG is a widely used biomarker for oxidative stress within cells and tissues,^{32,33} and participates in a variety of biological sequelae including photocleavage,³⁴ G-C \rightarrow A-T mutation,³⁵ Alzheimer's³⁶ and Parkinson's diseases,³⁷ and DNA–protein cross-linking.³⁸

The aforementioned $\text{G}^{\bullet+}$ kinetics indicate that free $\text{G}^{\bullet+}$ or that within ss DNA undergoes deprotonation overwhelmingly at neutral pH²⁸ (5 orders of magnitude faster than hydration), and produces little OG.³⁹ This, however, does not represent the scenario within ds DNA, where the hydration of $\text{G}^{\bullet+}$ becomes more efficient¹³ ($k = 6 \times 10^4 \text{ s}^{-1}$ at neutral pH⁴⁰) as $\text{G}^{\bullet+}$ is stabilized through base stacking and base pairing which limit its ability to lose a proton: *i.e.*, the N1-proton ($\text{p}K_{\text{a}} 3.9$)⁵ of $\text{G}^{\bullet+}$ is shared with the N3 ($\text{p}K_{\text{a}} 4.3$)⁴¹ of cytosine, with an equilibrium constant K_{eq} estimated to be 2.5 for $\text{G}^{\bullet+} \cdot \text{C} \rightleftharpoons [\text{G} - \text{H}]^\bullet \cdot [\text{C} + \text{H}]^+$. Consequently, the formation of OG in ds DNA is a factor of 7 greater than in ss DNA.²⁹ These seeming contradictions imply that free $\text{G}^{\bullet+}$ in solution might not faithfully mimic the local environment experienced by nucleobases within DNA.⁶ In this regard, a gas-phase environment may be more appropriate for examining $\text{G}^{\bullet+}$ structure and reactivity, as deprotonation

of $\text{G}^{\bullet+}$ shuts down in the gas phase and no longer competes with hydration.

$\text{G}^{\bullet+}$ is often generated by photolysis^{5,28,42} or radiolysis^{5,24,43} of $\text{S}_2\text{O}_8^{2-}$, Br^- or Cl^- solution where the resulting $\text{SO}_4^{\bullet-}$, $\text{Br}_2^{\bullet-}$ or $\text{Cl}_2^{\bullet-}$ in turn oxidized G to $\text{G}^{\bullet+}$, followed by measurements of radicals in solution or frozen/dry samples using transient absorption,^{25,28,29,42} IR,^{14,44} resonance Raman,⁴³ and EPR.^{24,30,31} Recently, the mechanistic aspects of the formation and subsequent deprotonation of $\text{G}^{\bullet+}$ in G-quadruplexes were examined in the presence of $\text{SO}_4^{\bullet-}$.^{45,46} Gas-phase $\text{G}^{\bullet+}$ could be formed by electron-impact ionization (EI) of guanine⁴⁷ or fast atom bombardment (FAB) of a mixture of guanosine and dimethoxynaphthalene in *m*-nitrobenzyl alcohol.⁴⁸ But EI and FAB generated substantial electronic and vibrational excitation and fragmentation of resulting radical ions. Pioneering work by Siu and co-workers⁴⁹ has shown that radical cations of tyrosyl-containing oligopeptides could be formed in the gas phase by collision-induced dissociation (CID) of $[\text{Cu}^{\text{II}}(\text{diethylenetriamine})(\text{oligopeptide})]^{2+}$ that was formed in solution and electrosprayed into the gas phase. Later, O'Hair and McFadyen *et al.* produced radical cations of nucleobases in a similar procedure using Cu^{II} ternary complexes of terpyridine and nucleobases/nucleosides.^{50,51} Recently, Cheng and Bohme⁵² and O'Hair and Orbell *et al.*⁵³ reported a more convenient way of producing nucleobase radical cations by CID of Cu^{II} –nucleoside binary complexes.

The successful generation of stable $\text{G}^{\bullet+}$ in the gas phase has made it possible to examine the intrinsic reactivity of $\text{G}^{\bullet+}$ unperturbed by solvent and counter ions. In the present work, reactions of water with radical cations of unsubstituted guanine ($9\text{HG}^{\bullet+}$, in an N9–H tautomeric form), 9-methylguanine ($9\text{MG}^{\bullet+}$), 2'-deoxyguanosine ($\text{dGuo}^{\bullet+}$) and guanosine ($\text{Guo}^{\bullet+}$) have been examined in the gas phase. We used tandem mass spectrometry coupled with ion-beam scattering to measure reaction cross sections, product branching ratios and their dependence on collision energy (E_{col}). The sensitivity of the gas-phase experiment, corroborated by reaction potential energy surface (PES) calculations and dynamics simulations, has led to a better understanding of guanine radical ion chemistry.

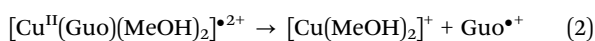
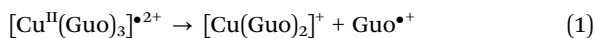
II. Experimental and computational details

1. Ion–molecule scattering

Reactions were carried out on a home-made electrospray ionization (ESI) guided-ion-beam tandem mass spectrometer described in detail elsewhere.⁵⁴ The apparatus consists of an ESI ion-source, a radio frequency (rf) hexapole ion guide, a quadrupole mass filter, an rf octopole ion guide surrounded by a scattering cell, a second quadrupole mass filter, and a pulse-counting electron multiplier detector. Both quadrupoles use Extrel 9.5 mm diameter tri-filter rods operating at 2.1 MHz to cover a mass/charge (m/z) range of 1–500.

Right before the experiment, a sample solution was prepared in methanol/water (3:1 vol) containing 0.25 mM

$\text{Cu}(\text{NO}_3)_2$ (Alfa Aesar, >99.999%) and 0.5 mM guanosine (Acros, 99%). The solution was sprayed into the ambient atmosphere through an electrospray needle at a flow rate of 0.06 mL h^{-1} , with an ESI potential of 2.35 kV relative to ground. Positively charged droplets entered the source chamber of the mass spectrometer through a pressure-reducing desolvation capillary. The distance between the emission tip of the ESI needle and the sampling orifice of the capillary was 7 mm. The capillary was biased at 115 V and heated to a temperature tuned between 180 and 200 °C to maximize desired ion intensities. Liquid aerosols underwent desolvation as they passed through the capillary, converting to a mixture of gas-phase doubly charged $[\text{Cu}^{\text{II}}(\text{Guo})_{0-6}(\text{MeOH})_{0-3}]^{2+}$.^{52,53} Ions were focused toward the capillary axis by gas flow and then transported into the source chamber that was evacuated to a pressure of 1.7 Torr. A skimmer with an orifice of 1.5 mm was located 3 mm away from the capillary end, separating the source chamber and the hexapole ion guide. The skimmer was biased at 17–25 V relative to ground. The electrical field between the capillary and the skimmer prompted CID of $[\text{Cu}^{\text{II}}(\text{Guo})_{0-6}(\text{MeOH})_{0-3}]^{2+}$ with background gas within the chamber, in which the fragmentation of $[\text{Cu}^{\text{II}}(\text{Guo})_3]^{2+}$ and $[\text{Cu}^{\text{II}}(\text{Guo})(\text{MeOH})_2]^{2+}$ features the production of $\text{Guo}^{\bullet+}$ *via* redox charge separation followed by dissociation due to Coulombic repulsion within the complex, and the resulting $\text{Guo}^{\bullet+}$ may rupture the *N*-glycosidic bond and produce $9\text{HG}^{\bullet+}$, *i.e.*, reactions (1)–(3):^{52,53}



$9\text{MG}^{\bullet+}$ and $\text{dGuo}^{\bullet+}$ were generated *via* in-source CID of $[\text{Cu}^{\text{II}}(9\text{MG})_3]^{2+}$ and $[\text{Cu}^{\text{II}}(\text{dGuo})_3]^{2+}$, for which the ESI solution was prepared using a mixing of 0.25 mM $\text{Cu}(\text{NO}_3)_2$ and 0.5 mM 9MG (Aldrich, $\geq 98.0\%$) or dGuo (Sigma, >99%).

Radical cations that emerged from the skimmer were transported into the hexapole ion guide at a pressure of 24 mTorr, undergoing collisional focusing and thermalization to $\sim 310 \text{ K}$. Radical cations subsequently passed into the first quadrupole mass filter for selection of specific radical ions. Mass-selected radical ions were collected and collimated by a lens set. The combination of collisional damping within the hexapole and the controlled collection radius at the quadrupole exit produced a mass-selected ion beam with a narrow kinetic energy spread. Mass-selected reactant ions were injected into the octopole ion guide, which trapped ions in the radial direction. The octopole was surrounded by the scattering cell. D_2O (Magnisolv, 99.9%) was held in a thermostated glass reservoir, purified by freeze–pump–thaw cycles before the experiment, and leaked into the scattering cell through a leak valve. The valve was kept at 80 °C to avoid freezing D_2O in the valve orifice. The scattering cell pressure was controlled at less than 0.08 mTorr (unless otherwise stated) and measured by a capacitance manometer (MKS 690 head and 670 signal conditioner). Under these conditions, reactant radical cations underwent at most a single collision with D_2O . A DC bias voltage was applied to the

octopole, allowing control of the kinetic energy of reactant ions in the laboratory frame (E_{Lab}) and thus of the E_{col} between reactant ions and D_2O molecules in the center-of-mass frame using $E_{\text{col}} = E_{\text{Lab}} \times m_{\text{neutral}}/(m_{\text{ion}} + m_{\text{neutral}})$, where m_{neutral} and m_{ion} are the masses of neutral and ionic reactants, respectively. After passing through the scattering cell, remaining reactant ions and product ions drifted to the end of the octopole, and then were m/z analyzed by the second quadrupole and counted by the electron multiplier.

The intensities of the reactant ion beam were $3\text{--}5 \times 10^5$ counts per s for $9\text{HG}^{\bullet+}$ and $9\text{MG}^{\bullet+}$, and $1.2\text{--}1.5 \times 10^5$ counts per s for $\text{dGuo}^{\bullet+}$ and $\text{Guo}^{\bullet+}$. The initial kinetic energy of the ion beam was set to 0.9 eV with an energy spread of 0.6 eV that corresponds to an E_{col} resolution of better than 0.07 eV. Reaction cross sections were calculated from the ratios of reactant and product ion intensities, the D_2O pressure in the scattering cell, and the effective cell length. The experiment was repeated multiple times and cycled through different E_{col} each time. Based on the reproducibility of the measurements, the relative error of the reaction cross sections (*e.g.* the uncertainty in comparing data at different E_{col}) was estimated to be $\leq 20\%$.

2. Electronic structure calculations

Density functional theory (DFT) has been extensively used for calculating the structures and reactions of nucleobase and nucleoside radical cations in the gas phase^{3,15,16,27,53,55–58} and in solution.^{15,16,56,57,59} Compared to B3LYP that suffers from spin-contamination for doublet systems²⁷ and self-interaction errors (SIE), ωB97XD ⁶⁰ mitigates SIE and improves the orbital descriptions of ionized states.⁵⁸ Therefore, reactants, intermediates, transition states (TSS) and products were calculated using ωB97XD paired with the 6-31+G(d,p) basis set. Conformation search was conducted for reactant ions, and their lowest-energy conformers were used as starting structures in PESs and dynamics simulations. TSS were verified as first-order saddle points, and the vibrational mode associated with an imaginary frequency corresponds to the anticipated reaction pathway. Aside from local criteria, intrinsic reaction coordinate (IRC) calculations were carried out to verify reactant/product minima connected through the TSS.

The ωB97XD -predicted stability order of conformers was confirmed by MP2/6-31+G(d,p). To benchmark the accuracy of $\omega\text{B97XD}/6\text{-}31\text{+G(d,p)}$ energies, we calculated AIEs for 9HG and 9MG and gas-phase acidities (GA) for $9\text{MG}^{\bullet+}$. $\omega\text{B97XD}/6\text{-}31\text{+G(d,p)}$ -calculated AIEs are 7.69 eV for 9HG and 7.53 eV for 9MG. For comparison, other predications are 7.65–7.68 eV (9HG) and 7.49 eV (9MG) at B3LYP/6-31+G(d,p),^{3,15,16} 7.71 eV (9HG) and 7.53 eV (9MG) at $\omega\text{B97XD}/6\text{-}31\text{+G(d)}$, 7.79 eV (9HG) and 7.64 eV (9MG) at M06-2X/6-31+G(d),⁵⁸ 7.82 eV (9HG) at MP2/6-311+G(d,p),⁶¹ 7.65 eV (9HG) at CASPT2(IPEA = 0.25)//CASSCF/ANO-L 431/21,⁶² and 7.89 eV (9HG) at G3MP2B3-ROMP2;⁶³ and the VUV photoionization-measured AIE is 7.75 eV for 9HG.³ The $\omega\text{B97XD}/6\text{-}31\text{+G(d,p)}$ -calculated GA of $9\text{MG}^{\bullet+}$ is $967.8 \text{ kJ mol}^{-1}$. The value was refined to $950.8 \text{ kJ mol}^{-1}$ by single-point calculation at DLPNO-CCSD(T)/aug-cc-pVTZ (the domain based local pair-natural orbital coupled-cluster method

with single-, double- and perturbative triple excitations⁶⁴) using ω B97XD optimized geometries. The latter value is in an excellent agreement with the experimental value of $952 \pm 10 \text{ kJ mol}^{-1}$ measured using Cooks' kinetic method.⁶⁵ Encouraged by the improved accuracy of this combination method, reaction enthalpies ($\Delta_r H^\circ$ at 298 K, with respect to reactants) were determined on the basis of electronic energies calculated at DLPNO-CCSD(T)/aug-cc-pVTZ// ω B97XD/6-31+G(d,p) and thermal corrections calculated at ω B97XD/6-31+G(d,p). The ω B97XD vibrational frequencies and zero-point energies (ZPEs) were scaled by factors of 0.95 and 0.974,⁶⁶ respectively. DFT and MP2 calculations were carried out using Gaussian 09,⁶⁷ and DLPNO-CCSD(T) calculations and T1 diagnostics were accomplished using ORCA 3.0.3.⁶⁸ Complex lifetimes were analyzed on the basis of Rice–Ramsperger–Kassel–Marcus (RRKM) theory,⁶⁹ for which unimolecular rate constants were calculated using the program of Zhu and Hase.⁷⁰

3. Direct dynamics trajectory simulations

Collision dynamics of 9HG^+ and 9MG^+ with water were simulated at $E_{\text{col}} = 0.1 \text{ eV}$, using the Venus software^{71,72} to set up trajectory initial conditions, and the Hessian-based predictor-corrector algorithm⁷³ implemented in Gaussian 09 to integrate the classical equations of motion, with the Hessian matrix updated every five steps. The initial separation between the centers of mass of randomly oriented collision partners was set at 8.0 \AA (where the attractive potential between reactants is negligible), with a collision impact parameter of 0 \AA . The vibrational and rotational temperatures of the reactants were set at 300 K to mimic the ion–molecule experiment. Quasi-classical Boltzmann sampling⁷⁴ was used to select vibrational and rotational energies. A quadratically convergent SCF method was used in case the conventional first-order SCF algorithm failed to converge. Trajectories were terminated when the product separation exceeded 8.8 \AA or the maximum trajectory integration time (5000 fs) was reached.

ω B97XD/6-31+G(d) was used for the simulations as it provided similar calculation accuracy to ω B97XD/6-31+G(d,p) but at less computational cost. 100 trajectories were accomplished for each of $9\text{HG}^+ + \text{H}_2\text{O}$ and $9\text{MG}^+ + \text{H}_2\text{O}$. Trajectories of 9HG^+ each took ~ 4300 CPU hours on an Intel 2.6 GHz core-based computational cluster, while those of 9MG^+ each took ~ 6100 CPU hours. Trajectories of representative collisions were recalculated at ω B97XD/6-31+G(d,p) to test how a basis set with the explicit polarization term for H affects trajectory outcomes. The ω B97XD/6-31+G(d,p) trajectories reproduced the collision dynamics observed at ω B97XD/6-31+G(d), and the difference between the two sets of trajectories is within statistical uncertainty. gOpenMol⁷⁵ was used for trajectory visualization. Individual trajectories and ensemble averages were analyzed using programs written for these purposes.

III. Results

1. Structures of radical cations

We have examined all low-lying structures of 9HG^+ , 9MG^+ , dGuo^+ and Guo^+ , taking into account the N9H–N7H tautomerization

of guanine and the *anti*- and *syn*-conformations about the *N*-glycosidic bond of dGuo^+ and Guo^+ . Their structures (Fig. S1–S4) and Cartesian coordinates are provided in the ESI.† All structures have no spin contamination ($\langle S^2 \rangle = 0.750$, as expected for a radical), and the T1 values from the CCSD(T) calculations did not exceed the upper limit of 0.02 (above which non-dynamic correlation effects are large enough to make the single-reference method unreliable).⁷⁶

Guanine has N9–H and N7–H tautomers, of which 7HG^+ lies in energy at least 0.11 eV above 9HG^+ and thus is unimportant. The global minima of 9HG^+ , 9MG^+ , dGuo^+ and Guo^+ all adopt a keto-conformation for the guanine moiety. The sugar groups of dGuo^+ and Guo^+ prefer an *anti*-keto configuration, opposite to the *syn*-enol conformation found for gas-phase neutral dGuo ⁷⁷ and Guo .⁷⁸ The calculated lowest-energy structures are consistent with IR spectra and CID of gas-phase 9MG^+ ⁶⁵ and dGuo^+ .^{53,55} On the basis of their populations at 298 K, these lowest-energy conformers should be overwhelmingly dominant in our experiment and were thus used in the discussion of reactions.

To demonstrate the location of the unpaired electron, spin density contours for the lowest-energy 9HG^+ , 9MG^+ , dGuo^+ and Guo^+ are plotted in Fig. 1, along with charge distributions. For comparison, both keto and enol conformers are included in the figure. All radical cations share the same spin density distribution in that an unpaired electron is delocalized among N3, C5 and C8. Charge is separated from spin and C8–H is more positively charged than other groups, making this site vulnerable to nucleophilic water attack. An obvious consequence of the substitution of N9–H is reflected in the charge densities: *i.e.*, the negative charge on N9 decreases from -0.38 at 9HG^+ to -0.11 at 9MG^+ , -0.06 at dGuo^+ and -0.04 Guo^+ ; meanwhile the charge on C4 changes from $+0.10$ at 9HG^+ to -0.07 at 9MG^+ , -0.25 at dGuo^+ and -0.26 at Guo^+ . Charges on C6 and C8 also change at dGuo^+ and Guo^+ . We tend to attribute these changes to hyperconjugation and the associated electron delocalization between the π bonds of guanine and the σ bond of the substituent. When the dihedral angle of C4–N9–C1'–O(sugar) is distorted from the original -121° to 0° so that the $\sigma(\text{C1}'\text{–O})$ bond lies perpendicular to the π orbitals, changes in the charge distributions become less substantial.

2. Reaction products, enthalpies and cross sections

The radical cations + D_2O isotope combination was used in the experiment to look for possible atom scrambling. For all four reactant ions, major product channels include the formation of water complexes (*i.e.*, hydration), H/D exchange (H/D_Exchange) and water-assisted keto–enol isomerization, as shown in reactions (4)–(7) where the presence of deuterium is indicated. H/D exchange and keto–enol isomerization have the same product ion mass. For the reaction of 9HG^+ , product ions were observed for H elimination (HE), *i.e.*, reaction (4d). Reaction enthalpies $\Delta_r H^\circ$ (298 K) were obtained from DLPNO-CCSD(T)/aug-cc-pVTZ// ω B97XD/6-31+G(d,p) calculations, and those for H/D exchange were calculated from

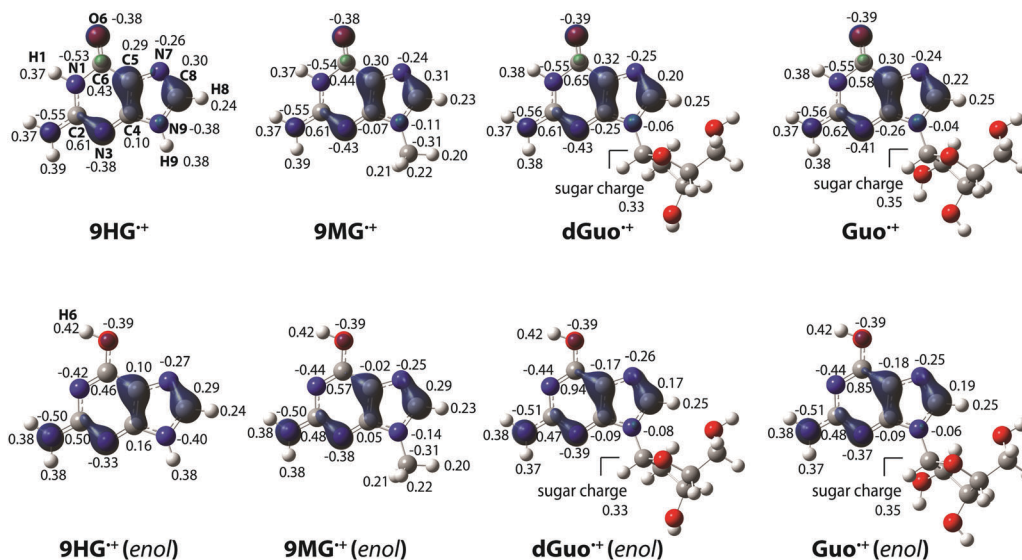
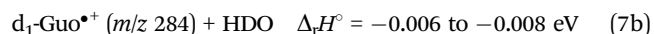
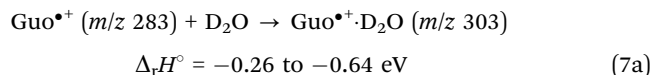
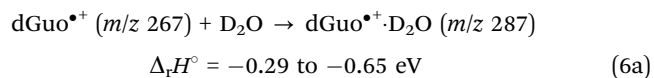
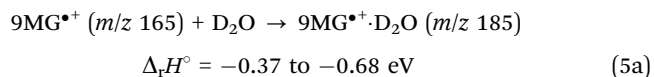
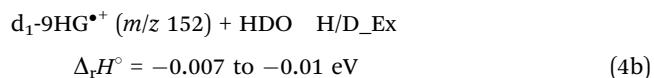
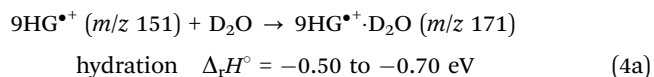


Fig. 1 Lowest-lying keto and enol conformers of 9HG^+ , 9MG^+ , dGuo^+ and Guo^+ . Atomic numbering schemes are presented. Spin (contour plots) and charge densities (numbers) were calculated at $\omega\text{B97XD}/6\text{-}31+\text{G}(\text{d},\text{p})$. Energies (eV) of enols vs. ketos were evaluated at $\text{DLPNO-CCSD}(\text{T})/\text{aug-cc-pVTZ}/\omega\text{B97XD}/6\text{-}31+\text{G}(\text{d},\text{p})$ with 298 K thermal corrections.

ZPE changes with deuteration occurring at different H positions.



In the experiments, all hydration products were formed under single hit conditions where a reactant ion reacts with water once or not at all; therefore the geometries of mono-hydrated products were predicted by adding a water molecule

to all possible hydration sites⁷⁹ of the reactant radical cations and then optimizing at $\omega\text{B97XD}/6\text{-}31+\text{G}(\text{d},\text{p})$. The optimized hydration structures are summarized in Fig. 2, in which the hydration sites are specified in the notation. The range of $\Delta_r H^\circ$ listed for the hydration reactions indicates the formation of all possible hydration structures, including W12a (*i.e.*, water hydrogen-bonded to N1-H and N2-H2a), W16, W9 and W2b for $9\text{HG}^+\cdot\text{H}_2\text{O}$, and W12a, W16, W2b and W8 (or W85') for $9\text{MG}^+\cdot\text{H}_2\text{O}$, $\text{dGuo}^+\cdot\text{H}_2\text{O}$ and $\text{Guo}^+\cdot\text{H}_2\text{O}$. $\text{dGuo}^+\cdot\text{H}_2\text{O}$ and $\text{Guo}^+\cdot\text{H}_2\text{O}$ have additional sugar-hydrated structures. It was found that the water ligand has no obvious influence on the spin and charge densities of the radical cations. An attempt was made to optimize complex structures where water is hydrogen-bonded to the lone-pair electron at N3 or N7, but none of these structures converged to stable complexes. Neither were such structures found in direct dynamics simulations (*vide infra*).

Reaction cross sections for individual product channels are shown in Fig. 3. Error bars were estimated by the variations between multiple experimental data sets. Reactions at E_{col} less than 0.1 eV produced very slow product ions that could not be collected efficiently due to potential barriers in the ion guide. Therefore, reaction cross sections were reported over a center-of-mass E_{col} range from 0.1 to 2.0 eV. To increase HE product ion intensity, a relatively high D_2O pressure (~ 0.2 mTorr) was used in the scattering cell; as a result, both single ($\sim 20\%$) and multiple ($\sim 8\%$) collisions have contributed to the measured HE cross section. Fig. 3c shows HE only for $9\text{HG}^+ + \text{D}_2\text{O}$, as the cross sections for the other three reaction systems are too small to measure the E_{col} dependence. What could be confirmed qualitatively is that all systems had H elimination at the lowest E_{col} , which should be mostly attributed to multiple collisions. The total reaction efficiency can be calculated as the ratio of $\sigma_{\text{total}}/\sigma_{\text{capture}}$, where σ_{capture} is the ion-neutral dipole capture cross section determined using the statistical adiabatic channel model.⁸⁰

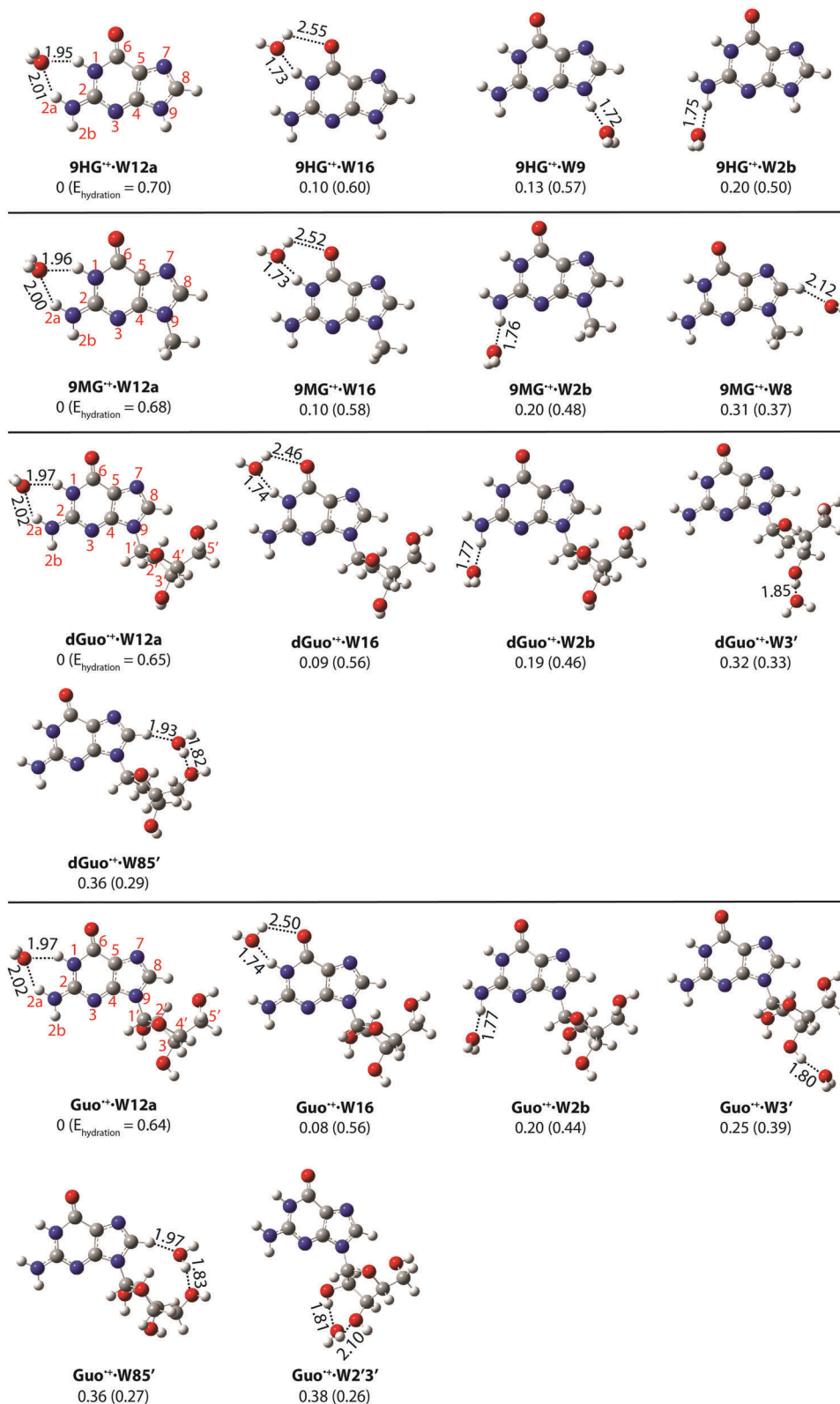


Fig. 2 Mono-hydrates of 9HG⁺⁺, 9MG⁺⁺, dGuo⁺⁺ and Guo⁺⁺. Atom numbering scheme and nomenclature are presented. Hydration sites are indicated by the last two numbers in the notation, and hydrogen bonds are depicted by dashed lines with lengths shown in Å. Relative energies (eV, with respect to global minima) and hydration enthalpies (in parentheses) were evaluated for all-H systems at DLPNO-CCSD(T)/aug-cc-pVTZ// ω B97XD/6-31+G(d,p) with 298 K thermal corrections. A D₂O ligand increases hydration enthalpy by ≤ 0.01 eV.

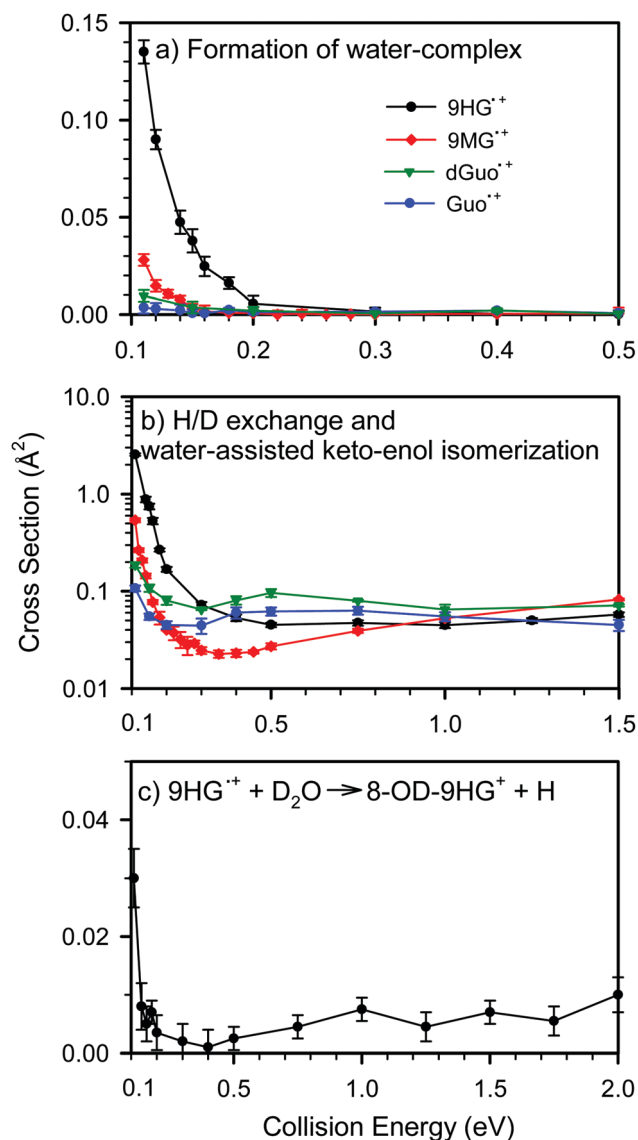


Fig. 3 Product cross sections for the reactions of D_2O with $9\text{HG}^{\bullet+}$, $9\text{MG}^{\bullet+}$, $\text{dGuo}^{\bullet+}$ and $\text{Guo}^{\bullet+}$ as a function of center-of-mass collision energy.

The efficiencies at the lowest E_{col} are 2% for $9\text{HG}^{\bullet+}$, 0.45% for $9\text{MG}^{\bullet+}$, 0.15% for $\text{dGuo}^{\bullet+}$ and 0.1% for $\text{Guo}^{\bullet+}$.

No proton transfer reaction of $\text{G}^{\bullet+} + \text{D}_2\text{O} \rightarrow [\text{G} - \text{H}]^{\bullet+} + \text{HD}_2\text{O}^+$ was seen at E_{col} up to 2.0 eV, since the reaction was calculated to be endothermic by 2.81, 2.64, 2.86 or 2.73 eV when the proton is abstracted from guanine N1, N2a, N2b or N9, respectively. Neither did we observe the hydrogen abstract reaction of $\text{G}^{\bullet+} + \text{D}_2\text{O} \rightarrow [\text{G} + \text{D}]^{\bullet+} + \text{OD}^{\bullet}$, as the reaction is 1.70 eV endothermic and thus disfavored in the present E_{col} range.

3. Trajectory results

For a complex system, use of chemical intuition to predict reaction pathways may prove unreliable as there exist multiple concurrent and competing processes. Therefore, direct dynamics trajectories were calculated for $9\text{HG}^{\bullet+} + \text{H}_2\text{O}$ and $9\text{MG}^{\bullet+} + \text{H}_2\text{O}$ at $E_{\text{col}} = 0.1$ eV (100 trajectories for each). Dynamics simulations explore multiple

minima in the conformation landscape and the reaction PES. The motion of molecules is followed, allowing the molecules to show what the preferred reaction pathways are.^{73,81–84} Of the 200 trajectories we have simulated, 31.5% can be characterized as direct, nonreactive scattering, resulting in conversion of some E_{col} into vibrational and rotational energies. The remaining trajectories first form electrostatic complexes upon collisions. Such collision complexes do not have well-defined geometries or directional hydrogen bonds. They are simply floppy complexes of reactants, with large-amplitude intermolecular motion. The importance of these complexes, referred to as precursors in the remainder of discussion, is that they allow repeated encounters between reactants, increasing the probability of eventually locking into a stable hydrogen bond such as W12a. Still, a large fraction of precursors dissociate to reactants before the end of the trajectories.

Two representative trajectories for forming $9\text{MG}^{\bullet+} \cdot \text{H}_2\text{O}$ are illustrated in Fig. 4a and b, where each frame shows collision time scale, changes in system potential energy (PE) and the centers-of-mass distance between collision partners, and changes in hydrogen bonds along the trajectory. In the trajectory of Fig. 4a, the collision instant is around 300 fs; after that a precursor forms and then converges to a W12a structure at 1000 fs, as shown by the formation of rH1–water and rH2a–water hydrogen bonds in the bottom frame. The two gray levels within the bottom frame mark the maximum distances for weak and modest interactions, respectively. The oscillations in the PE and bond lengths reflect molecular vibrations (including ZPE) and intermolecular motions. The trajectory in Fig. 4b represents the formation of a W8 complex. Note that W8 forms only in the trajectories of $9\text{MG}^{\bullet+} + \text{H}_2\text{O}$, and the nature of W8 is more electrostatic attraction than a hydrogen bond.

Our trajectory simulation times (~ 5 ps) were too short compared to the ion time-of-flight within the mass spectrometer; therefore we could not predict the distribution of complex structures in the final product ions as most of the complexes would eventually be driven by the acquired hydration enthalpy to dissociate, and some trajectories may inter-convert between different hydrogen bonds. The purpose of our dynamics simulations was to examine reaction dynamics at the early stage — the point in the reaction coordinate where different product channels and the effects of reactant structure originate. To this end, formation probabilities of different complex structures in the trajectories of $9\text{HG}^{\bullet+} + \text{H}_2\text{O}$ and $9\text{MG}^{\bullet+} + \text{H}_2\text{O}$ are compared in the histograms of Fig. 4c. The overall height of each column represents the total formation probability of individual structures, and the white area represents the fraction of complexes that dissociate to starting reactants before the end of the trajectories.

W12a was observed in both $9\text{HG}^{\bullet+} + \text{H}_2\text{O}$ and $9\text{MG}^{\bullet+} + \text{H}_2\text{O}$ trajectories, as the most probable structure in complex forming. W12a also has the strongest hydrogen bond among all hydration structures, according to the DFT calculations in Fig. 2. Surprisingly, the yield of W16 is minor in both $9\text{HG}^{\bullet+}$ and $9\text{MG}^{\bullet+}$ trajectories, despite it representing the second strongest hydrogen bond. In sharp contrast, W8 diminishes in the

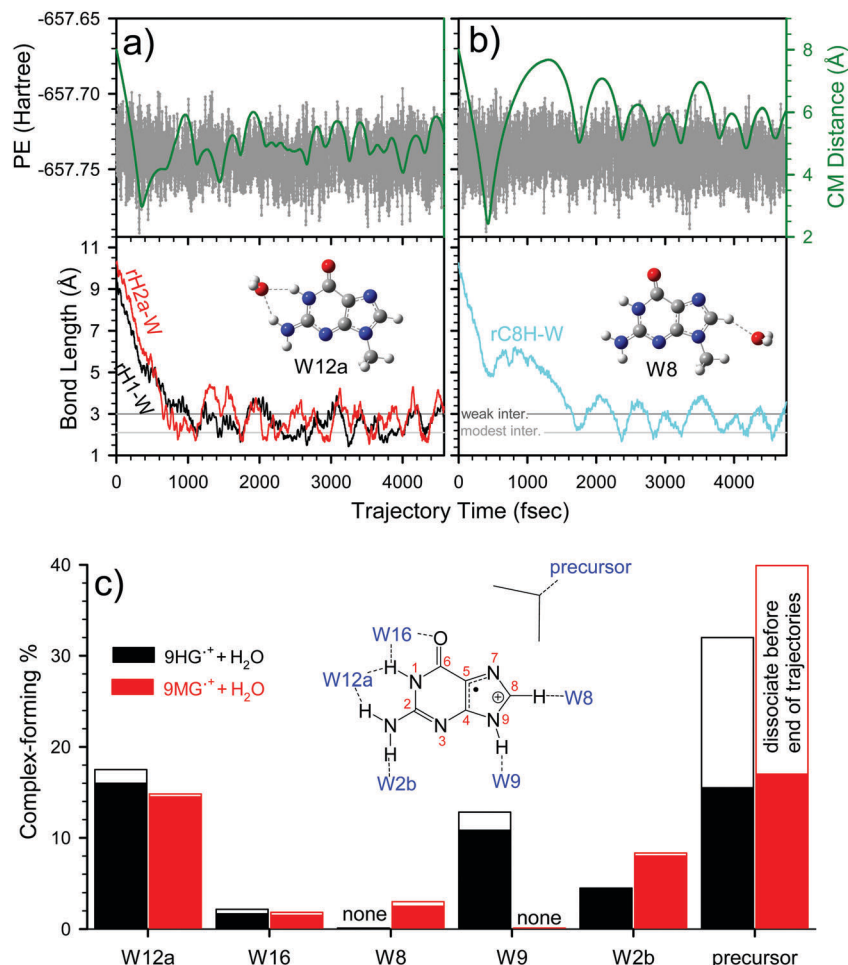


Fig. 4 (a and b) Representative complex-forming trajectories for $9\text{MG}^{\bullet+} + \text{H}_2\text{O}$, simulated at $E_{\text{col}} = 0.1$ eV. Each set shows the changes in PE and the CM separation between collision partners (right axis), and the formation of hydrogen bonds; and (c) formation probabilities of different complex structures in the trajectories of $9\text{HG}^{\bullet+} + \text{H}_2\text{O}$ and $9\text{MG}^{\bullet+} + \text{H}_2\text{O}$. Distribution probabilities are based on 100 trajectories for each system.

trajectories of $9\text{HG}^{\bullet+} + \text{H}_2\text{O}$, whereas W9 diminishes in $9\text{MG}^{\bullet+} + \text{H}_2\text{O}$. As mentioned above, W8 is more an electrostatic complex than hydrogen-bonded. We tried to optimize a W8-like structure for $9\text{HG}^{\bullet+} \cdot \text{H}_2\text{O}$, but the water always swings out of the original position and is directed to a W9 structure. To compensate for the lack of a W9 structure, $9\text{MG}^{\bullet+} + \text{H}_2\text{O}$ forms much more W2b and precursor than $9\text{HG}^{\bullet+} + \text{H}_2\text{O}$. The overall complex formation efficiencies are 69% for $9\text{HG}^{\bullet+} + \text{H}_2\text{O}$ and 68% for $9\text{MG}^{\bullet+} + \text{H}_2\text{O}$; but $9\text{MG}^{\bullet+} + \text{H}_2\text{O}$ produces more precursors (40%) than $9\text{HG}^{\bullet+} + \text{H}_2\text{O}$ (32%), and consequently presents a higher dissociation rate: *i.e.*, 35% of $9\text{MG}^{\bullet+} \cdot \text{H}_2\text{O}$ dissociate before the end of the trajectories, and the rate drops to 30% for $9\text{HG}^{\bullet+} \cdot \text{H}_2\text{O}$.

IV. Discussion

1. Hydration complexes, H/D exchange and keto-enol isomerization

Despite the fact that the formation of water complexes is energetically most favorable, water complexes were detected

only at low E_{col} and even then $\sigma_{\text{Hydration}}$ is at most 5% of the total cross section. We have calculated the lifetimes of various water complexes using the RRKM theory. For the decay of these complexes to reactants, orbiting transition states⁸⁵ were assumed because there are no reverse barriers. In the calculations, we used average angular momenta corresponding to capture cross sections, *i.e.*, $L = \mu \cdot \nu_{\text{rel}} \cdot (\sigma_{\text{capture}}/\pi)^{1/2}$, where μ and ν_{rel} are the reduced mass and relative velocity of collision partners, respectively. The recoil energy needed to calculate orbiting TSs was estimated from dynamics trajectories. The average lifetime of $9\text{HG}^{\bullet+} \cdot \text{H}_2\text{O}$ is 70–80 ns at $E_{\text{col}} = 0.1$ eV, dropping to 3 ns at 0.2 eV and 0.1 ns at 0.5 eV. $9\text{MG}^{\bullet+} \cdot \text{H}_2\text{O}$ is longer lived than $9\text{HG}^{\bullet+} \cdot \text{H}_2\text{O}$, with an average lifetime of 1 μs at $E_{\text{col}} = 0.1$ eV, 60 ns at 0.2 eV and 2 ns at 0.5 eV. The longest lived complexes correspond to $\text{dGuo}^{\bullet+} \cdot \text{H}_2\text{O}$ and $\text{Guo}^{\bullet+} \cdot \text{H}_2\text{O}$. Their lifetimes are > 10 μs at $E_{\text{col}} = 0.1$ eV, 0.5 μs at 0.2 eV and 3 ns at 0.5 eV. The RRKM results imply that the lifetimes of all water complexes are shorter than the ion time-of-flight (μs) in the mass spectrometer, and most complexes decayed back to reactants before reaching the ion detector. The mass spectrometer collected only a very small fraction of hydration products.

The dominant product channel for all reactant ions is H/D exchange. Note that keto–enol isomerization could only be observed in the experiment if there was concomitant H/D exchange. An obvious question is the extent to which simple H/D scrambling (without structure rearrangement) and keto–enol isomerization each contribute to the product cross section, and how their contributions vary with E_{col} . Our experiment could not distinguish which guanine tautomer formed in the products, but has provided clues through the reaction E_{col} -dependence. At low energies H/D exchange is strongly suppressed by E_{col} , and its cross section approaches a minimum at $E_{\text{col}} = 0.2\text{--}0.4$ eV. However, starting from 0.3 eV the cross section rebounds, becoming energy-independent toward the high E_{col} limit. Such E_{col} dependence suggests that H/D exchange is dominated by one mechanism at the lowest E_{col} , while a second mechanism grows at high E_{col} . The low-energy H/D exchange is most likely mediated by a complex and proceeds *via* hydrogen migration or isomerization of hydrogen bonds, with the formation probability and/or lifetime of such migrated complexes strongly suppressed by E_{col} . A complex-mediated H/D exchange at low E_{col} is consistent with the same dependence of complex-forming and H/D exchange cross sections on reactant ion structures (see Fig. 3a and b). The endothermic keto–enol isomerization may contribute to low-energy reactions, but cannot be dominant as judged from the E_{col} -inhibiting feature of the reaction. The high-energy mechanism, on the other hand, can be mostly attributed to water-assisted keto–enol isomerization. The PES for reaction (4c) is depicted in Fig. 5. There are many complexes formed in collisions, but reaction (4c) must certainly pass through W16. The TS for isomerization can be characterized as double proton transfers occurring simultaneously, with an activation barrier 0.53 eV above $9\text{HG}^+\cdot\text{W16}$, but still 0.07 eV below the reactants. Catalyzed by

water, the reaction has a threshold of only 0.06 eV. Keto–enol isomerization may also be possible for dry radical cations *via* a direct N1-to-O6 proton transfer. We have calculated TS(no water) in Fig. 5 for the direct version of keto–enol isomerization. The barrier rises to 1.69 eV above the starting reactants, rendering the isomerization of dry guanine less likely. Similar water-assisted isomerization was observed for a neutral 8-hydroxyl guanine radical.⁸⁶

The above discussion leads to the following picture of the dynamics: (1) at low energies, a set of short-lived water complexes form, and before dying out a fraction of them mediate H/D exchange; (2) as E_{col} rises, the probability of complex forming decreases rapidly. It is more reasonable to assume that keto–enol isomerization occurs in an already correctly oriented (W16-like) structure allowing for double proton transfer, by which we mean that reactivity is controlled by collision geometry; (3) as an additional note, $\text{dGuo}^+\cdot\text{H}_2\text{O}$ and $\text{Guo}^+\cdot\text{H}_2\text{O}$ can carry the water ligand for a longer time than $9\text{HG}^+\cdot\text{H}_2\text{O}$ and $9\text{MG}^+\cdot\text{H}_2\text{O}$ at high E_{col} (a phenomenon that could be rationalized in terms of increased degrees of freedom and more efficient IVR in large systems), among which the W16 structure could catalyze keto–enol isomerization. This is supported by the experimental observation that H/D exchange for dGuo^+ and Guo^+ does not undergo as steep a decrease as 9HG^+ and 9MG^+ when E_{col} starts to increase, and has higher $\sigma_{\text{H/D,EX}}$ than 9HG^+ and 9MG^+ at high energies. Of course, a direct mechanism still dominates for dGuo^+ and Guo^+ at high energies.

2. C8-hydroxylation and H elimination

Perhaps the biologically most relevant product channel is water attack at the C8 position of guanine radical cations, as this is the first step toward the cascade of the OG lesions. Despite its pivotal role, the C8-adduct $[\text{8-OH-G} + \text{H}]^+$ has never been

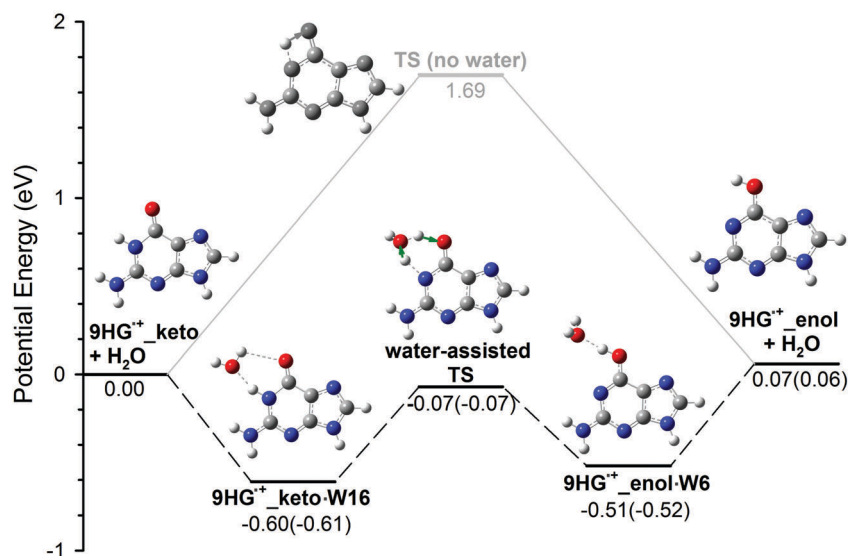


Fig. 5 PES for keto–enol isomerization of 9HG^+ in the presence and the absence of water. Reaction enthalpies (eV, for all-H species) were determined on the basis of electronic energies at DLPNO-CCSD(T)/aug-cc-pVTZ// $\omega\text{B97XD}/6\text{-}31\text{+G(d,p)}$, and 298 K thermal corrections at $\omega\text{B97XD}/6\text{-}31\text{+G(d,p)}$. For TSs, vibrational modes corresponding to imaginary frequencies are indicated by displacement vectors. Numbers in parentheses are reaction enthalpies with D_2O .

directly detected except by EPR/ENDOR measurement of OH[•] addition to solid N7-protonated guanine.³¹ Schuster and co-worker⁸⁷ reported an experiment on the reaction of water with dGuo^{•+} in DNA. In the experiment, hydrophobic alkyl-substituted cytidines and thymidines were incorporated into the duplex, by which they had expected to repel the otherwise tightly bound water molecules in their vicinity and disrupt the hydration of dGuo^{•+}. The experiment did not produce noticeable changes. Later, they found that a counter ion located in the DNA major groove in proximity to the GG segment could assist the addition of water to ionized DNA.⁸⁸

We were able to detect H-elimination products in the reaction of 9HG^{•+} + D₂O, which we tend to attribute to a C8-adduct-mediated reaction on the basis of the PES calculation in Fig. 6. The PES is presented for all-H species to allow comparison with the literature (and the differences in reaction enthalpies for deuterated species are less than 0.01 eV). Under single ion-molecule collision conditions, the HE reaction corresponds to 9HG^{•+} + H₂O → 9HG^{•+}·W → TS1-W (C8-water addition) → [8-OH-9HG + H]^{•+} (formation of C8-hydroxylated intermediate) → TS2 (H elimination) → 8-OH-9HG^{•+} + H. 9HG^{•+}·W can be characterized as reactants-like with an intermolecular distance of 2.9 Å. The complex is electrostatically bonded, and it is unlikely that there would be an activation barrier to its formation. The rate-limiting steps correspond to two tighter activation barriers, TS1-W and TS2, with the maximum barrier height being 1.42 eV above the reactants. There is another charge state

for the HE products: *i.e.*, 8-OH-G[•] + H⁺, for which the reaction enthalpy is 9.53 eV and thus was not considered further.

The calculated HE endothermicity is consistent with our experimental observation that the HE cross section increases at high E_{col} . The fact that HE is minor even at high energies could be partially explained by inter-product channel competition, and partially by the suppression by angular momentum conservation.⁸⁹ The reduced mass for HE products is 20 times lower than that for H/D exchange; thus for a given recoil angular momentum, the centrifugal barrier will be roughly an order of magnitude larger. In other words, it was more difficult for the HE products to escape over the centrifugal barrier than for the H/D products. Because H/D exchange itself is a minor channel at high E_{col} , a factor of 20 suppression would shut down HE for 9MG^{•+}, dGuo^{•+} and Guo^{•+}.

Our PES for single-water addition to the C8 of 9HG^{•+} agrees with the repulsive reactant interaction reported by Reynisson and Steenken;²⁷ however, we have identified a non-repulsive reaction route when two water molecules are added to the reaction. As shown by the blue lines in Fig. 6, the second water significantly lowers TS1 for C8-water addition (by 1.4 eV) and there is no barrier for water nucleophilic addition. Videos for the IRC trajectories crossing TS1-W and TS1-2W are available in the ESI,[†] giving intuitive pictures of single- and double-water reactions with 9HG^{•+}. TS1-2W features an activation structure where a bond between C8 and a water O atom forms concurrently with the transfer of a water proton towards a neighboring

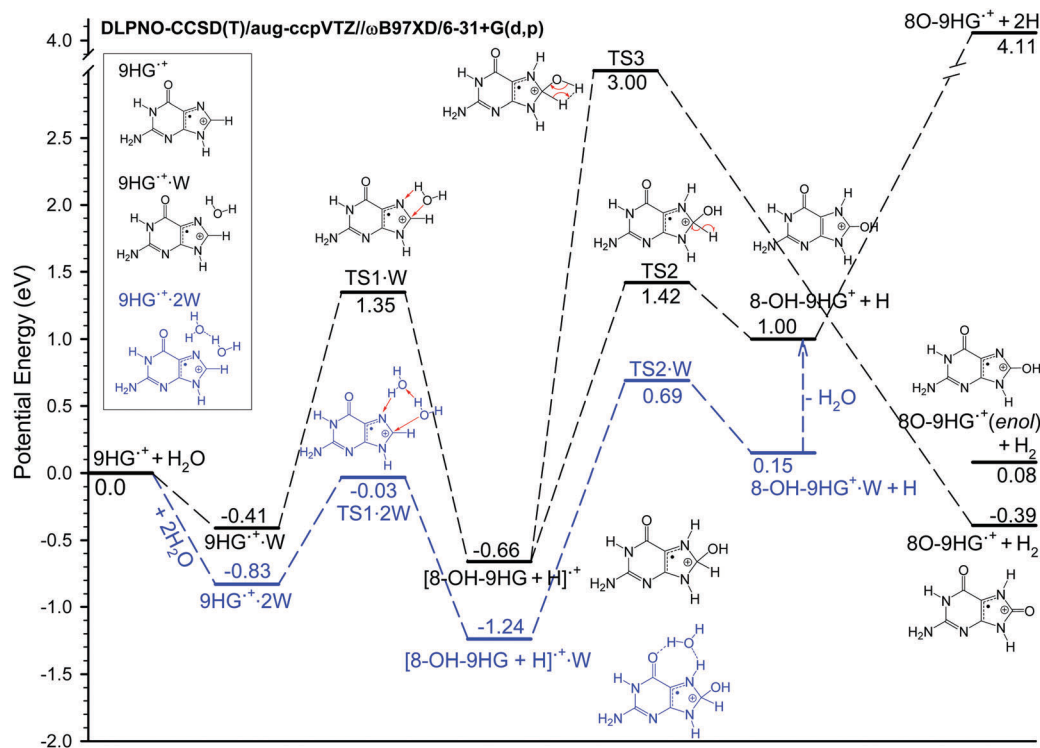


Fig. 6 PES for C8-water addition to 9HG^{•+}. Reaction enthalpies (eV, for all-H species) were determined by the sum of electronic energies calculated at DLPNO-CCSD(T)/aug-cc-pVTZ// ω B97XD/6-31+G(d,p), and 298 K thermal corrections at ω B97XD/6-31+G(d,p). Structures of TS2-W and 8-OH-9HG^{•+}·W are similar to their dry analogues except for a water bonded to N7-H and C6-O. Trajectories (in MP4 format) for 9HG^{•+} + H₂O → TS1-W → [8-OH-9HG + H]^{•+} and 9HG^{•+} + 2H₂O → TS1-2W → [8-OH-9HG + H]^{•+} + H₂O are available in the ESI.[†]

water molecule, and the latter water then transfers a proton to N7. The “second water-assisted C8-water addition” is reminiscent of the counter ion-assisted water addition reported by Schuster and co-worker.⁸⁸ In both cases, the activation barrier diminishes for a reaction that starts from a configuration where a proton (in our experiment) or an Na⁺ (in Schuster *et al.*'s) resides at or near the N7 of a guanine radical cation and evolves through a TS incorporating a proton shuttle mechanism. The formation of 9HG^{•+}·2W and TS1·2W provides an explanation for the HE cross section observed at the lowest E_{col} (Fig. 3c), where the combination of long collision time and high D₂O pressure made multiple collisions (up to 8%) and thus three-body reactions possible.

Lastly, we have computed two pathways leading from [8-OH-9HG + H]^{•+} to 8O-9HG^{•+}: one is consecutive elimination of two H atoms, *i.e.*, [8-OH-9HG + H]^{•+} → TS2 → 8-OH-9HG⁺ + H → 8O-9HG^{•+} + 2H, and the other is concerted H₂ elimination from C8-H and C8-OH, *i.e.*, [8-OH-9HG + H]^{•+} → TS3 → 8O-9HG^{•+} + H₂. Both pathways require high activation energy (>3 eV) and thus are not feasible in the experiment. We have explored the possibility of forming an enol isomer of 8O-9HG^{•+} (0.47 eV higher in energy than keto) *via* H₂ elimination from N7-H and C8-H of [8-OH-9HG + H]^{•+}; however, no TS could be located. Alternatively, the enol-isomer could be interconverted directly from 8O-9HG^{•+}, and the accompanying transition state is 2.29 eV above 8O-9HG^{•+}.

3. The effects of N9-substitution

9HG^{•+}, 9MG^{•+}, dGuo^{•+} and Guo^{•+} have similar reaction enthalpies and activation barriers. On the basis of the DFT-predicted hydrogen-bonding structures in Fig. 2, one may image that dGuo^{•+} and Guo^{•+} would offer the deoxyribose/ribose OH groups for additional hydrogen bonding, such as W3' and W85', and form more water complexes. The striking observation is that 9HG^{•+} seems the most hydrophilic, while all of the N9-substituents inhibit both complex formation and H/D exchange at low energies. The fact that the low- E_{col} cross sections of 9MG^{•+}, dGuo^{•+} and Guo^{•+} are comparable to each other but much lower than that of 9HG^{•+} implies that the hydroxyl groups of deoxyribose and ribose have not participated in hydration, at least not to a significant extent. Related to this observation is that Saigusa and co-workers reported similar mono-hydrated structures of dGuo and Guo, from which they have ruled out the hydration of 2'-OH.⁹⁰ The same group reported that the lowest-energy structure of Guo·H₂O is analogous to that of 9MG·H₂O.⁹¹

Since the hydration of the sugar moiety has been ruled out in our reactions and the DLPNO-CCSD(T)/ωB97XD calculations have indicated that the methyl, 2'-deoxyribose and ribose groups make little difference to reaction enthalpies and activation barriers, we can therefore use 9HG^{•+} + H₂O *vs.* 9MG^{•+} + H₂O as model systems to capture the physics of the collisions and to delineate the dynamics influence of N9-substituents. The reaction E_{col} -dependence and the trajectory simulations have confirmed that low-energy reactions are complex-mediated; thus the lack of a W9 structure seems to be the most likely reason for the reduced reactivity of N9-substituted radical

cations. By comparing reaction cross sections and the product branching of 9HG^{•+} + H₂O and 9MG^{•+} + H₂O at 0.1 eV, we may estimate that 9HG^{•+}·W9 may account for ~75% of detected water complexes. On the other hand, the yield of W12a in the final products may not be as significant as it has been shown to be in the trajectories (*cf.* Fig. 4c); otherwise we would have expected a lower decrease for 9MG^{•+}, dGuo^{•+} and Guo^{•+}. The implication is that, in addition to complex formation, reactions involve dynamics factors such as complex lifetimes and orientation. In addition, the formation of W16 was found to be modest in the trajectories. In light of this result, we restate that keto–enol isomerization is dominated by a direct mechanism, and the contribution of W16-mediated keto–enol isomerization should be modest.

V. Summary

The guided ion-beam scattering experiment, reaction PES calculations and dynamics simulations were carried out to discover the mechanism and dynamics for the attack by water on guanine radical cations in the gas phase where the deprotonation of the guanine radical cation is blocked. Various N9-substituted guanine radical cations were examined including 9HG^{•+}, 9MG^{•+}, dGuo^{•+} and Guo^{•+}, in the order of increasing structural complexity. At low E_{col} , the collisions lead to many short-lived complexes with various hydrogen bonds, of which a W9 structure with water hydrogen-bonded to N9-H acts as an important intermediate. The substitution of N9-H blocks the formation of W9, and no hydration of guanosine sugar hydroxyl groups was observed. A combination of these factors results in decreasing reactivity in the order 9HG^{•+} > 9MG^{•+} > dGuo^{•+} ≈ Guo^{•+}. At high E_{col} , water-catalyzed keto–enol isomerization dominates that occurs by a direct mechanism, except that for dGuo^{•+} and Guo^{•+} where the relatively long-lived W16 complexes may enhance isomerization. Despite being a minor product channel, the most biologically relevant product ions, 8-OH-9HG⁺ (a critical intermediate in the post-ionization conversion of guanine nucleobase into OG), were captured in the reaction of 9HG^{•+} with water. It was found that C8-water nucleophilic addition has a high activation barrier in the presence of only a single water molecule, but the barrier vanishes once a second water molecule is added to the reaction as a catalyst. It would be interesting to explore the effects of adding more water molecules to the reaction system. Understanding the dynamics of a multiply-hydrated radical system is more challenging, and thus has more intimate biological relevance since the biological reaction environment presents more complex hydrogen bonding structures. Instead of speculating, we plan to simulate the dynamics of two- and three-water-participating C8-hydroxylation in future work. Two simulation approaches will be utilized: the first is to model the reactions of mono-hydrated 9MG^{•+}·H₂O + H₂O and dihydrated 9MG^{•+}·(H₂O)₂ + H₂O, with specific hydrogen bonds in 9MG^{•+}·H₂O and 9MG^{•+}·(H₂O)₂ reactant ions and one of the water ligands specifically attached to C8-H; and the other is to follow the

trajectories evolving from TS1-2W that connect the reactant and the C8-hydroxylated product, so that more insight can be acquired into the dynamics of the reactions of interest.

Conflicts of interest

There are no conflicts to declare.

Acknowledgements

This work was supported by the National Science Foundation (Grant No. CHE 1464171), CUNY PSC-CUNY Award and Queens College Research Enhancement Award.

References

- 1 S. Steenken and S. V. Jovanovic, *J. Am. Chem. Soc.*, 1997, **119**, 617–618.
- 2 C. J. Burrows and J. G. Muller, *Chem. Rev.*, 1998, **98**, 1109–1151.
- 3 J. Zhou, O. Kostko, C. Nicolas, X. Tang, L. Belau, M. S. de Vries and M. Ahmed, *J. Phys. Chem. A*, 2009, **113**, 4829–4832.
- 4 M. Schwell and M. Hochlaf, *Top. Curr. Chem.*, 2015, **355**, 155–208.
- 5 L. P. Candeias and S. Steenken, *J. Am. Chem. Soc.*, 1989, **111**, 1094–1099.
- 6 S. Steenken, *Chem. Rev.*, 1989, **89**, 503–520.
- 7 L. P. Candeias and S. Steenken, *J. Am. Chem. Soc.*, 1992, **114**, 699–704.
- 8 D. N. Nikogosyan, *Int. J. Radiat. Biol.*, 1990, **57**, 233–299.
- 9 I. Saito, T. Nakamura and K. Nakatani, *J. Am. Chem. Soc.*, 2000, **122**, 3001–3006.
- 10 E. D. A. Stemp and J. K. Barton, *Met. Ions Biol. Syst.*, 1996, **33**, 325–365.
- 11 H. H. Thorp, *Trends Biotechnol.*, 1998, **16**, 117–121.
- 12 C. Ribaut, G. Bordeau, P. Perio, K. Reybier, V. Sartor, O. Reynes, P.-L. Fabre and N. Chouini-Lalanne, *J. Phys. Chem. B*, 2014, **118**, 2360–2365.
- 13 H. Kasai, Z. Yamaizumi, M. Berger and J. Cadet, *J. Am. Chem. Soc.*, 1992, **114**, 9692–9694.
- 14 J. P. Hall, F. E. Poynton, P. M. Keane, S. P. Gurung, J. A. Brazier, D. J. Cardin, G. Winter, T. Gunnlaugsson, I. V. Sazanovich, M. Towrie, C. J. Cardin, J. M. Kelly and S. J. Quinn, *Nat. Chem.*, 2015, **7**, 961–967.
- 15 T. Caruso, M. Carotenuto, E. Vasca and A. Peluso, *J. Am. Chem. Soc.*, 2005, **127**, 15040–15041.
- 16 C. E. Crespo-Hernández, D. M. Close, L. Gorb and J. Leszczynski, *J. Phys. Chem. B*, 2007, **111**, 5386–5395.
- 17 F. D. Lewis, X. Liu, J. Liu, S. E. Miller, R. T. Hayes and M. R. Wasielewski, *Nature*, 2000, **406**, 51–53.
- 18 J. Cadet, M. Berger, G. W. Buchko, P. C. Joshi, S. Raoul and J.-L. Ravanat, *J. Am. Chem. Soc.*, 1994, **116**, 7403–7404.
- 19 L. P. Candeias and S. Steenken, *Chem. – Eur. J.*, 2000, **6**, 475–484.
- 20 J. Cadet, T. Douki and J.-L. Ravanat, *Acc. Chem. Res.*, 2008, **41**, 1075–1083.
- 21 W. L. Neeley and J. M. Essigmann, *Chem. Res. Toxicol.*, 2006, **19**, 491–505.
- 22 O. R. Alshykhly, A. M. Fleming and C. J. Burrows, *J. Org. Chem.*, 2015, **80**, 6996–7007.
- 23 A. M. Fleming and C. J. Burrows, *Free Radical Biol. Med.*, 2017, **107**, 35–52.
- 24 A. Adhikary, A. Kumar, D. Becker and M. D. Sevilla, *J. Phys. Chem. B*, 2006, **110**, 24171–24180.
- 25 K. Kobayashi and S. Tagawa, *J. Am. Chem. Soc.*, 2003, **125**, 10213–10218.
- 26 K. Kobayashi, R. Yamagami and S. Tagawa, *J. Phys. Chem. B*, 2008, **112**, 10752–10757.
- 27 J. Reynisson and S. Steenken, *Phys. Chem. Chem. Phys.*, 2002, **4**, 527–532.
- 28 Y. Rokhlenko, N. E. Geacintov and V. Shafirovich, *J. Am. Chem. Soc.*, 2012, **134**, 4955–4962.
- 29 Y. Rokhlenko, J. Cadet, N. E. Geacintov and V. Shafirovich, *J. Am. Chem. Soc.*, 2014, **136**, 5956–5962.
- 30 K. Hildenbrand and D. Schulte-Frohlinde, *Free Radical Res. Commun.*, 1990, **11**, 195–206.
- 31 S. D. Wetmore, R. J. Boyd and L. A. Eriksson, *J. Phys. Chem. B*, 1998, **102**, 9332–9343.
- 32 H. Sies, *Oxidative Stress*, Academic Press, 1985.
- 33 S. Boiteux and J. P. Radicella, *Biochimie*, 1999, **81**, 59–67.
- 34 B. Armitage, *Chem. Rev.*, 1998, **98**, 1171–1200.
- 35 S. D. Bruner, D. P. G. Norman and G. L. Verdine, *Nature*, 2000, **403**, 859–866.
- 36 M. A. Lovell and W. R. Markesbery, *Arch. Neurol.*, 2001, **58**, 392–396.
- 37 J. Zhang, G. Perry, M. A. Smith, D. Robertson, S. J. Olson, D. G. Graham and T. J. Montine, *Am. J. Pathol.*, 1999, **154**, 1423–1429.
- 38 X. Xu, J. G. Muller, Y. Ye and C. J. Burrows, *J. Am. Chem. Soc.*, 2008, **130**, 703–709.
- 39 T. Douki, S. Spinelli, J.-L. Ravanat and J. Cadet, *J. Chem. Soc., Perkin Trans. 2*, 1999, 1875–1880.
- 40 B. Giese and M. Spichty, *ChemPhysChem*, 2000, **1**, 195–198.
- 41 J. A. Dean, *Lange's Handbook of Chemistry, Fifteenth Edition*, McGraw-Hill, New York, 1999.
- 42 L. Wu, K. Liu, J. Jie, D. Song and H. Su, *J. Am. Chem. Soc.*, 2015, **137**, 259–266.
- 43 J. Choi, C. Yang, M. Fujitsuka, S. Tojo, H. Ihee and T. Majima, *J. Phys. Chem. Lett.*, 2015, **6**, 5045–5050.
- 44 A. W. Parker, C. Y. Lin, M. W. George, M. Towrie and M. K. Kuimova, *J. Phys. Chem. B*, 2010, **114**, 3660–3667.
- 45 T. J. Merta, N. E. Geacintov and V. Shafirovich, *Photochem. Photobiol.*, 2018, DOI: 10.1111/php.12926.
- 46 Y. Yang, H. Su, W. Fang, X. Chen and W. Yang, *Phys. Chem. Chem. Phys.*, 2018, **20**, 13598–13606.
- 47 J. M. Rice and G. O. Dudek, *J. Am. Chem. Soc.*, 1967, **89**, 2719–2725.
- 48 A. Liguori, A. Napoli and G. Sindona, *J. Am. Soc. Mass Spectrom.*, 2001, **12**, 176–179.

- 49 I. K. Chu, C. F. Rodriguez, T.-C. Lau, A. C. Hopkinson and K. W. M. Siu, *J. Phys. Chem. B*, 2000, **104**, 3393–3397.
- 50 S. Wee, R. A. J. O'Hair and W. D. McFadyen, *Rapid Commun. Mass Spectrom.*, 2005, **19**, 1797–1805.
- 51 A. K. Y. Lam, B. F. Abrahams, M. J. Grannas, W. D. McFadyen and R. A. J. O'Hair, *Dalton Trans.*, 2006, 5051–5061.
- 52 P. Cheng and D. K. Bohme, *J. Phys. Chem. B*, 2007, **111**, 11075–11082.
- 53 L. Feketeová, E. Yuriev, J. D. Orbell, G. N. Khairallah and R. A. J. O'Hair, *Int. J. Mass Spectrom.*, 2011, **304**, 74–82.
- 54 Y. Fang and J. Liu, *J. Phys. Chem. A*, 2009, **113**, 11250–11261.
- 55 L. Feketeová, B. Chan, G. N. Khairallah, V. Steinmetz, P. Maître, L. Radom and R. A. J. O'Hair, *Phys. Chem. Chem. Phys.*, 2015, **17**, 25837–25844.
- 56 N. Agnihotri and P. C. Mishra, *J. Phys. Chem. B*, 2009, **113**, 3129–3138.
- 57 A. Yadav and P. C. Mishra, *Int. J. Quantum Chem.*, 2012, **112**, 2000–2008.
- 58 A. Kumar and M. D. Sevilla, *J. Phys. Chem. B*, 2014, **118**, 5453–5458.
- 59 B. T. Psciuk and H. B. Schlegel, *J. Phys. Chem. B*, 2013, **117**, 9518–9531.
- 60 J.-D. Chai and M. Head-Gordon, *Phys. Chem. Chem. Phys.*, 2008, **10**, 6615–6620.
- 61 E. Caueet, D. Dehareng and J. Lievin, *J. Phys. Chem. A*, 2006, **110**, 9200–9211.
- 62 D. Roca-Sanjuán, M. Rubio, M. Merchán and L. Serrano-Andrés, *J. Chem. Phys.*, 2006, **125**, 084302.
- 63 L. Zhang, Y. Pan and F. Qi, *J. Theor. Comput. Chem.*, 2009, **8**, 1103–1115.
- 64 D. G. Liakos, M. Sparta, M. K. Kesharwani, J. M. L. Martin and F. Neese, *J. Chem. Theory Comput.*, 2015, **11**, 1525–1539.
- 65 L. Feketeová, G. N. Khairallah, B. Chan, V. Steinmetz, P. Maître, L. Radom and R. A. J. O'Hair, *Chem. Commun.*, 2013, **49**, 7343–7345.
- 66 I. M. Alecu, J. Zheng, Y. Zhao and D. G. Truhlar, *J. Chem. Theory Comput.*, 2010, **6**, 2872–2887.
- 67 M. J. Frisch, G. W. Trucks, H. B. Schlegel, G. E. Scuseria, M. A. Robb, J. R. Cheeseman, G. Scalmani, V. Barone, B. Mennucci, G. A. Petersson, H. Nakatsuji, M. Caricato, X. Li, H. P. Hratchian, A. F. Izmaylov, J. Bloino, G. Zheng, J. L. Sonnenberg, M. Hada, M. Ehara, K. Toyota, R. Fukuda, J. Hasegawa, M. Ishida, T. Nakajima, Y. Honda, O. Kitao, H. Nakai, T. Vreven, J. J. A. Montgomery, J. E. Peralta, F. Ogliaro, M. Bearpark, J. J. Heyd, E. Brothers, K. N. Kudin, V. N. Staroverov, T. Keith, R. Kobayashi, J. Normand, K. Raghavachari, A. Rendell, J. C. Burant, S. S. Iyengar, J. Tomasi, M. Cossi, N. Rega, J. M. Millam, M. Klene, J. E. Knox, J. B. Cross, V. Bakken, C. Adamo, J. Jaramillo, R. Gomperts, R. E. Stratmann, O. Yazyev, A. J. Austin, R. Cammi, C. Pomelli, J. W. Ochterski, R. L. Martin, K. Morokuma, V. G. Zakrzewski, G. A. Voth, P. Salvador, J. J. Dannenberg, S. Dapprich, A. D. Daniels, O. Farkas, J. B. Foresman, J. V. Ortiz, J. Cioslowski and D. J. Fox, *Gaussian 09, Revision D.01*, Gaussian, Inc, Wallingford, CT, 2013.
- 68 F. Neese, *Wiley Interdiscip. Rev.: Comput. Mol. Sci.*, 2012, **2**, 73–78.
- 69 R. A. Marcus, *J. Chem. Phys.*, 1952, **20**, 359–364.
- 70 L. Zhu and W. L. Hase, *A general RRKM program (QCPE 644), Quantum chemistry program exchange*, Chemistry Department, University of Indiana, Bloomington, 1993.
- 71 X. Hu, W. L. Hase and T. Pirraglia, *J. Comput. Chem.*, 1991, **12**, 1014–1024.
- 72 W. L. Hase, K. Bolton, P. de Sainte Claire, R. J. Duchovic, X. Hu, A. Komornicki, G. Li, K. Lim, D. Lu, G. H. Peslherbe, K. Song, K. N. Swamy, S. R. Vande Linde, A. Varandas, H. Wang and R. J. Wolf, *VENUS 99: A general chemical dynamics computer program*, Texas Tech Univeristy Lubbock, TX, 1999.
- 73 V. Bakken, J. M. Millam and H. B. Schlegel, *J. Chem. Phys.*, 1999, **111**, 8773–8777.
- 74 G. H. Peslherbe, H. Wang and W. L. Hase, *Adv. Chem. Phys.*, 1999, **105**, 171–201.
- 75 L. Laaksonen, gOpenMol, Center for Scientific Computing, Espoo, Finland, 3.0 edn., 2005, available at www.csc.fi/gopenmol/.
- 76 T. J. Lee and P. R. Taylor, *Int. J. Quantum Chem., Quantum Chem. Symp.*, 1989, **36**, 199–207.
- 77 E. Nir, I. Huenig, K. Kleinermanns and M. S. de Vries, *ChemPhysChem*, 2004, **5**, 131–137.
- 78 H. Asami, S.-h. Urashima, M. Tsukamoto, A. Motoda, Y. Hayakawa and H. Saigusa, *J. Phys. Chem. Lett.*, 2012, **3**, 571–575.
- 79 H. Saigusa, N. Mizuno, H. Asami, K. Takahashi and M. Tachikawa, *Bull. Chem. Soc. Jpn.*, 2008, **81**, 1274–1281.
- 80 J. Troe, *Chem. Phys. Lett.*, 1985, **122**, 425–430.
- 81 *Advances in classical trajectory methods, Intramolecular and nonlinear dynamics*, ed. W. L. Hase, JAI, Greenwich, 1998, vol. 1.
- 82 M. Döntgen, M.-D. Przybylski-Freund, L. C. Kröger, W. A. Kopp, A. E. Ismail and K. Leonhard, *J. Chem. Theory Comput.*, 2015, **11**, 2517–2524.
- 83 E. Martínez-Núñez, *Phys. Chem. Chem. Phys.*, 2015, **17**, 14912–14921.
- 84 S. Pratihar, X. Ma, Z. Homayoon, G. L. Barnes and W. L. Hase, *J. Am. Chem. Soc.*, 2017, **139**, 3570–3590.
- 85 M. T. Rodgers, K. M. Ervin and P. B. Armentrout, *J. Chem. Phys.*, 1997, **106**, 4499–4508.
- 86 P. Liu, C. Li, S. Wang and D. Wang, *J. Phys. Chem. B*, 2018, **122**, 3124–3132.
- 87 F. O. Onyemauwa and G. B. Schuster, *Photochem. Photobiol.*, 2006, **82**, 729–732.
- 88 R. N. Barnett, A. Bongiorno, C. L. Cleveland, A. Joy, U. Landman and G. B. Schuster, *J. Am. Chem. Soc.*, 2006, **128**, 10795–10800.
- 89 H.-T. Kim, J. Liu and S. L. Anderson, *J. Chem. Phys.*, 2001, **115**, 1274–1286.
- 90 H. Asami, S.-H. Urashima and H. Saigusa, *Phys. Chem. Chem. Phys.*, 2009, **11**, 10466–10472.
- 91 H. Saigusa, S.-h. Urashima and H. Asami, *J. Phys. Chem. A*, 2009, **113**, 3455–3462.